1 **Data Repository**

2

3 **for**

4

5 Unraveling the complexity of deep gas accumulations with 3D multimodal CARS

6 microscopy

7

8 Robert C. Burruss[1]

9 Aaron D. Slepkov[2]

10 Adrian F. Pegoraro[2,3]

11 Albert Stolow[2,3]

12

13 [1]U.S. Geological Survey, Reston, VA, USA

14 [2]Steacie Institute for Molecular Sciences, National Research Council, Ottawa, ON,

15 Canada

16 [3]Department of Physics, Queen's University, Kingston, ON, Canada

17

18

19
20

21

22 **Samples**

23   Fluid inclusions were analyzed in the five samples listed in Table DR1. The

24 samples are doubly-polished thin-sections that were prepared for microthermometric

25 measurements. With the exception of Sample 1, these are archival samples of studies in

26 which basic descriptive information has been previously published.

27

28 Table DR1: Sample information

29

Sample No.	Sample ID	Location information	Geologic setting	Host mineral	Reference
1	Bilger	Central Pennsylvania	Fracture-filling cement, Marcellus Formation	Quartz	Evans, M., unpublished
2	K-Ap	Eastern Pennsylvania	Fracture-filling cement, Devonian rocks	Quartz	(Kisch and van den Kerkhof, 1991)
3	G-STP-13	Western Maine	Siluro-Devonian metamorphic terrain	Quartz	(Burruss, 1977)
4	25-1-2	Southwest Indian Ridge, Indian Ocean	Oceanic plutonic rocks, layer 3 of ocean crust	Hornblende	(Vanko and Stakes, 1991)
5	FAF-1	North-central Arkansas	Septarian fracture-filling cement, Fayetteville Formation	Calcite	(Burruss, 1981)

30
31
32 **CARS Methodology and Image Processing**
33
34   Laser scanning nonlinear optical microscopy was implemented on a commercial

35 inverted microscope platform (Olympus FluoView 300), modified to allow non-

36 descanned signal collection in the forward direction through a multimode fiber (Slepkov

37 et al., 2011). The two-photon excitation fluorescence (TPEF) signal was isolated and

38 collected in the epi-direction with a built-in photomultiplier tube (PMT), and second

39   harmonic generation (SHG) and CARS signals were separated by wavelength with a

40   dichroic mirror and collected in the forward direction by separate PMTs. The imaging

41   objective was either a 40×, 1.15 NA water immersion lens, with coverslip correction

42   collar (Olympus, U Plan Apo IR) or a 40×, 0.8 NA water immersion dipping lens

43   (Olympus, LUMPlanFI). The forward scatter was collected with a long-working-distance

44   0.55 NA condenser.

45   Laser light for TPEF and SHG was provided by a tunable Ti:sapphire oscillator

46   (Coherent Inc., Mira 900) emitting 60 fs pulses at a repetition rate of 80 MHz and an

47   average power of 1.5 W. For CARS microscopy, 200 mW was split and coupled through

48   a commercial supercontinuum-generating photonic crystal fiber module (NKT Photonics,

49   FemtoWHITE CARS), and the subsequent 65 mW of output continuum was filtered by a

50   sequence of filters and a dichroic combiner to send 16 mW of >950 nm light comprised

51   our CARS "Stokes" beam to the microscope scan head. The remaining laser power—

52   comprising our CARS "pump" beam and our SHG and TPEF beam—was attenuated to

53   150–300 mW, and was combined on a 45º dichroic mirror (Chroma Technology 950dcxr)

54   with the Stokes pulses. By varying the path length for the pump pulses with a computer-

55   controlled retro-reflector stage, the relative temporal overlap between the pump and

56   Stokes pulses is scanned to yield the continuous CARS spectrum. Furthermore, the

57   insertion of 10 cm of SF6 glass in the joint pump and Stokes arms and an additional 5 cm

58   of SF6 glass in the Stokes arm stretches both pulses in time, and allows for the necessary

59   pulse shaping (chirp-matching (Hellerer et al., 2004)) to yield both 20 cm^{-1} resolution in

60   the CARS spectrum, and sufficient peak pulse intensity at the microscope focus to allow

61   for simultaneous SHG and TPEF imaging. Without the use of matched glass blocks, the

62   resolution of our femtosecond-laser based CARS spectra is nominally 200 cm^{-1}. Various

63   central wavelengths ranging from 795 nm to 826 nm were used for the data presented

64   herein. At a central wavelength of 800 nm, the SHG signal is generated at 400 nm, the

65   TPEF signal ranges from 650 nm to 450 nm, and the anti-Stokes (CARS signal) light

66   ranges from 649 nm at the C-H stretch peak at 2900 cm^{-1} to 639 nm at the O-H peak at

67   3150 cm^{-1}.

68   Regardless of the central wavelength of the Ti:sapphire oscillator used for these

69   experiments (ranging from 795 nm to 826 nm), the output supercontinuum of the

70   photonic crystal fiber module essentially remains constant in extent in the near-infrared,

71   ranging from 975 nm to 1175 nm. This light constitutes our Stokes beam. Throughout

72   this range, the spectral density of the Stokes beam varies considerably, and, in general, it

73   has the highest density between 1025 nm and 1060 nm, as described previously (Slepkov

74   et al., 2010). At a pump wavelength of 795 nm, the peak of the supercontinuum Stokes

75   spectral density covers the strong C-H vibrational band and most of the O-H vibrational

76   band. Thus, this wavelength was used for most methane- and water-inclusion imaging.

77   To effectively image nitrogen-bearing inclusions, the pump wavelength is tuned to 826

78   nm, where it mixes with the peak in the Stokes pulse to probe the N-N vibrational mode

79   at 2320 cm^{-1}, but where there is also sufficient spectral density in the Stokes beam to

80   fully probe the methane peak around 2910 cm^{-1}.

81   The "chirp rate" of a pulse describes how its wavelength varies in time. More

82   specifically, the chirp rate is the variation in frequency (energy) as a function of time

83   within the pulse. To obtain the best CARS spectral resolution within a given pump pulse

84   duration, the chirp rate of the pump and Stokes pulses must be identical. For the

85   experiments presented here, 15 cm of total SF6 glass is placed in the Stokes arm, and 10

86   cm of SF6 glass is present in the pump arm. This yields a measured spectral resolution

87   for CARS of 20 cm^{-1}, as shown by the line shape of the spectrum presented in Fig. 1(G).

88   Different frequency components overlap between the pump and Stokes arms depending

89   on the optical path length settings of the pump arm. This optical path length is varied to

90   overlap different frequency components between the Stokes and pump beams, and thus to

91   probe different vibrational frequencies. A retro-reflector on a computerized translation

92   stage is used to scan this delay (i.e. to scan the CARS spectrum). To calibrate the CARS

93   frequency scale, we directly measure the generated anti-Stokes spectrum as a function of

94   optical delay. By collecting the non-descanned anti-Stokes light in the forward direction

95   with a multimode fiber (Slepkov et al., 2011) we are able to send this signal to a portable

96   off-board spectrometer (Ocean Optics Inc.). Anti-Stokes central wavelength as a function

97   of delay stage position data, together with knowledge of the central pump pulse

98   wavelength can be converted to yield a calibration of CARS frequency as a function of

99   stage position. CARS signals in a glass slide pumped at 300 mW are used for this

100   purpose, because the response across the entire accessible frequency scale (2100 cm^{-1}–

101   4500 cm^{-1}) is nonresonant and largely unstructured. For the experimental conditions

102   described here a linear fit to the data yields a Stokes chirp rate of 414 cm^{-1}/ps (11 data

103   points; R^2=0.9994).

104   When the CARS microscope is operated in spectral-scanning mode, a single plane

105   of the sample is imaged and the CARS spectrum is built up at each pixel by scanning the

106   delay stage through the CARS resonance. Thus, for images in the manuscript where a

107   region of interest (ROI) is identified and a spectrum is shown, there is complete

108   hyperspectral information at each pixel (representing a volume of ~1 μm^3). The CARS

109   spectra for any given ROI are an average of the spectra of every pixel within the specified

110   ROI. We have not averaged any spectra at different depths within an image stack.

111

112   **CARS spectroscopy vs. Raman spectroscopy in geoscience applications**: There are

113   some key differences between spontaneous Raman scattering spectra and CARS spectra

114   that complicate their direct comparison. Two of these differences, peak shape and peak

115   intensity are inherent to the nonlinear optical processes that generate the CARS signal. A

116   third, the range of the CARS spectrum that can be recorded, is a function of our

117   implementation of CARS spectroscopy.

118   The peak shape is a function of the four-wave mixing nature of the CARS process

119   because the collected anti-Stokes light is a mixture of vibrationally-resonant light and

120   electronically-derived "nonresonant background" (Cheng et al., 2001). The relative

121   amount of one source to the other is determined by a host of experimental conditions—

122   unique to each particular experimental implementation of CARS—including spectral

123   resolution and excitation bandwidth, Raman resonance line width, and concentration of

124   resonant oscillators within the excitation volume (Ganikhanov et al., 2006; Pegoraro et

125   al., 2009). These features manifest themselves commonly as a reshaping of the

126   vibrational line shape on the high-energy side of a resonance, most often resulting in a

127   dip below the baseline and gradual return. This so-called dispersive line shape is a direct

128   effect of coherent addition of the electric fields of the nonresonant signal and the resonant

129   signal, which are out of phase on the high-energy side of the vibrational resonance. At

130   high resonant-to-nonresonant signal ratios, this reshaping diminishes and the line shape

131   approaches that of a Lorentizan, as in conventional Raman spectroscopy. The

132   nonresonant background in quartz is miniscule compared to the strength of the C-H

133   vibrational resonant signal in methane at our experimental conditions, and thus our

134   CARS spectra for methane in inclusions closely resemble traditional Raman spectra (but

135   currently limited to 20 cm^{-1} resolution), as seen in Fig. 1G. The Lorentzian fit to the

136   spectrum in Fig 1G is excellent on the low-energy side of the spectrum, but slightly

137   diminished on the high-energy side of the spectrum. These effects ultimately further

138   result in a slight bathochromic shift of the CARS peak compared to the Raman peak.

139   Indeed, we consistently find the strong C-H vibrational peak for methane at 2904–2910

140   cm^{-1}, as compared to 2914 cm^{-1} in spontaneous Raman scattering spectra.

141   In a conventional microfocused Raman spectrometer, the intensity of a Raman

142   band is a linear function of the number of molecules in the focal volume of the laser and a

143   linear function of the laser power. However, the nonlinear optical processes that generate

144   the CARS signal cause the signal to be a quadratic function of both the number of

145   molecules in the focal volume and the laser power. Furthermore, the baseline of the

146   spectrum is affected by the nonresonant background as discussed above. Therefore,

147   relatively weak scatterers or molecules at low concentration can yield very weak signals

148   in CARS, making resolution from background and quantitative calibration of intensity to

149   concentration difficult (Day et al., 2011). A conventional Raman microprobe can be

150   calibrated to quantitatively estimate the concentration of methane dissolved in the

151   aqueous phase of a 2-phase inclusion such as incl. #3 in Fig. 3B and Fig. DR1A (Dubessy

152   et al., 2001). However, as shown in the spectrum of the aqueous phase of incl. 3 in Fig.

153   DR1B our implementation of CARS spectroscopy cannot resolve a peak for CH$_4$

154   dissolved in the aqueous phase.   As the technology of microfocused CARS spectroscopy

155   and related stimulated Raman scattering methods evolve, quantitative calibration of these

156   methods may be possible (Day et al., 2011).

157   As noted in the text, the frequency range of CARS resonance that can be recorded

158   by our system is currently 2100 to 4500 cm^{-1}. This is a design limitation based on

159   optimization for biomedical imaging and spectroscopy of the C-H stretch of lipids and

160   the O-H stretch of water at the cellular level. This is not an inherent limitation of CARS.

161   Systems using lasers with different tuning ranges and different types of detectors have

162   been constructed for imaging and spectroscopy over the frequency range of 500 to 3500

163   cm^{-1} (Lee et al., 2011). However, each implementation of CARS involves tradeoffs in

164   frequency range, spectral resolution, speed of imaging, and multimodal imaging

165   capability, not to mention complexity and cost of the system. Our initial experiments

166   with a modified setup indicate that imaging CO_2-rich fluid inclusions is possible at 1284

167   and 1388 cm^{-1}, but further modifications are required to allow routine imaging.

168

169   **Manuscript images and image processing:** All nonlinear microscopy images were

170   acquired using the Olympus FluoView software, which synchronizes the laser scanners

171   (x-y), the objective position along the optical axis (z), and the acquisition from

172   photomultiplier tube (PMT) detectors. We typically obtain 256×256 pixel images,

173   especially when collecting hyperspectral images (x-y images + spectrum at each pixel),

174   but we occasionally collect 512×512 pixel images, particularly when collecting three-

175   dimensional volumes at a fixed CARS frequency. For hyperspectral imaging, the

176   computerized optical delay stage that scans the spectrum is synchronized with the

177   FluoView software by a custom-made user-defined LabView (National Instruments Inc.)

178   program that allows us to control the scan speed and spectral sampling rate. Typical 256

179   × 256 images are collected in 0.33 s (5 µs pixel dwell time). A hyperspectral scan, such

180   as shown in Figs. 1G and 3B takes approximately 3–6 minutes to collect. Data analysis

181   and further image processing is conducted in ImageJ (release 1.43u, in the public domain

182   from NIH), with an expanded set of plugins for 3D rendering and the "Intensity v Time

183   Monitor."

184

185   *Figure 1 processing.* Fig. 1B is a single slice snapshot from a three-dimensional

186   rendering rotation sequence shown in video DR1. The physical scan dimensions are 350

187   µm × 350 µm × 78 µm, obtained as a 512 × 512 × 78 voxel volume, each slice collected

188   as an average of 3 images. Two image stacks are obtained to yield the best contrast for

189   the purely resonant signal from methane; an "on resonance" sequence at 2910 cm^{-1}, and

190   an "off resonance" signal at 2700 cm^{-1}. These image stacks are then subtracted to yield

191   the purely resonant signal at 2910 cm^{-1}. The display settings were chosen for maximum

192   contrast, and thus represent the maximum volume of methane observable. Fig. 1C–1F)

193   represent a re-scan close-up of the inclusion labeled "i" in Fig. 1B. These were obtained

194   simultaneously as a spectral scan sequence of 279 256 × 256 images. Figs. 1C and 1D,

195   representing the SHG and TPEF response from the inclusions are averages of five

196   consecutive images taken at an arbitrary spectral position, whereas Fig. 1E is an average

197   of five consecutive images spanning the C-H peak centered at 2910 cm^{-1}, subtracted by

198   five consecutive images taken off resonance at 2700 cm^{-1}. The spectral data for Fig. 1G

199   were obtained by projecting the average signal from the selected region of interest (ROI)

200   shown in Fig. 1F across the hyperspectral scan stack.

201

202   *Figure 2 processing.* Fig. 2 is a single-slice snapshot from a three-dimensional rendering

203   rotation sequence shown in video DR2. The physical scan dimensions are 175 µm × 175

204   µm × 60 µm, obtained as a $512 \times 512 \times 60$ voxel volume, each slice collected as an

205   average of 3 images. For the CARS (red) channel, two image stacks are obtained to yield

206   the best contrast for the purely resonant signal from methane; an "on resonance"

207   sequence at 2910 cm^{-1}, and an "off resonant" signal at 3080 cm^{-1}. These image stacks are

208   then subtracted directly to yield only the purely resonant signal at 2910 cm^{-1}. The display

209   settings were chosen for heightened contrast. For the SHG (green) channel, signal was

210   collected simultaneously with CARS, and no processing was done aside from overlaying

211   it with the processed CARS channel data and adjusting the contrast settings for best

212   visualization.

213

214   *Figure 3 processing.* Fig. 3A is a 2D projection of a 3D volume stack of the CARS signal

215   from CH_4 and H_2O in Sample 2. A 3D rendering rotation sequence of this volume is

216   shown in video DR3. The physical scan dimensions are 78 µm × 78 µm × 44 µm,

217   obtained as a $512 \times 512 \times 88$ voxel volume, each slice collected as an average of 3

218   images. Three image stacks are obtained to yield the best contrast for the purely resonant

219   signal from methane and water; a "C-H resonance" sequence at 2910 cm^{-1}, a "O-H

220   resonance" sequence at 3230 cm^{-1}, and an "off resonant" signal at 2620 cm^{-1}. The "off

221   resonance" stack is subtracted from the "C-H resonance" stack to yield only the purely

222   resonant signal for methane (red). The "C-H resonance" stack is subtracted from the "O-

223   H resonance" stack to yield only the purely resonant signal for water (green). The display

224   settings were chosen for maximum contrast. For the 3D rotation rendering (video DR3) a

225   Gaussian blurring filter of 1 pixel diameter is used to reduce speckle and random noise.

226   No blurring was used for the image in Fig. 3A.

227

228   *Figure 4 processing.* Fig. 4A is an overlay of the CARS image collected at 2845 cm^{-1},

229   representing the peak signal from crude oil (red), and TPEF signal collected in the epi-

230   direction (green). These were obtained simultaneously as a spectral scan sequence of 298

231   256×256 images, with 55 µm $\times$ 55 µm scan dimensions and no averaging. For the

232   CARS signal (red), a sequential five-frame average taken at 3080 cm^{-1}, representing the

233   nonresonant signal, was subtracted from a sequential five-frame average taken across

234   2841–2848 cm^{-1}, to yield the best contrast for the purely resonant signal from crude oil at

235   2845 cm^{-1}. Fig. 4B shows the CARS spectra from an inclusion containing crude oil and

236   methane and from a bubble within the same inclusion that contains mostly methane and

237   some higher hydrocarbons. The raw spectra are averaged over the selected ROIs and are

238   normalized to the spectrum taken from the host matrix adjacent to the inclusions,

239   representing the nonresonant background.

240

241   **References**

242   Burruss, R. C., 1977, Analysis of fluid inclusions in graphitic metamorphic rocks from

243   Bryant Pond, Maine, and Khtada Lake, British Columbia: Thermodynamic basis

244   and geologic interpretation of observed fluid compositions and molar volumes

245   [Ph.D. thesis: Princeton University, 156 p.

246 Burruss, R. C., 1981, Hydrocarbon fluid inclusions in studies of sedimentary diagenesis,

247   *in* Hollister, L. S., and Crawford, M. L., eds., Short Course in Fluid Inclusions:

248   Applications to Petrology, Volume 6: Calgary, Mineralogical Association of

249   Canada, p. 138-156.

250 Cheng, J. X., Volkmer, A., Book, L. D., and Xie, X. S., 2001, An epi-detected coherent

251   anti-Stokes Raman scattering (E-CARS) microscope with high spectral resolution

252   and high sensitivity: Journal of Physical Chemistry B, v. 105, p. 1277-1280.

253 Day, J. P. R., Domke, K. F., Rago, G., Kano, H., Hamaguchi, H., Vartiainen, E. M., and

254   Bonn, M., 2011, Quantitative coherent anti-Stokes Raman scattering (CARS)

255   microscopy: Journal of Physical Chemistry B, v. 115, p. 7713-7725.

256 Dubessy, J., Buschaert, S., Lamb, W., Pironon, J., and Thiery, R., 2001, Methane-bearing

257   aqueous fluid inclusions: Raman analysis, thermodynamic modelling and

258   application to petroleum basins: Chemical Geology, v. 173, p. 193-205.

259 Ganikhanov, F., Evans, C. L., Saar, B. G., and Xie, X. S., 2006, High-sensitivity

260   vibrational imaging with frequency modulation coherent anti-Stokes Raman

261   scattering (FM CARS) microscopy: Optics Letters, v. 31, p. 1872-1874.

262 Hellerer, T., Enejder, A. M. K., and Zumbusch, A., 2004, Spectral focussing: high

263   spectral resolution spectroscopy with broad-bandwidth laser pulses: Applied

264   Physics Letters, v. 85, no. 25-27.

265 Kisch, H. J., and van den Kerkhof, A. M., 1991, CH_4-rich inclusions form quartz veins in

266   the Valley-and-Ridge province and the anthracite fields of the Pennsylvania

267   Appalachians: American Mineralogist, v. 76, p. 230-240.

268 Lee, Y. J., Moon, D., Migler, K. B., and Cicerone, M. T., 2011, Quantitative image

269   analysis of broadband CARS hyperspectral images of polymer blends: Analytical

270   Chemistry, v. 83, p. 2733-2739.

271 Liu, Y., Lee, Y. J., and Cicerone, M. T., 2009, Broadband CARS spectral phase retrieval

272   using a time-domain Kramers-Kronig transform: Optics Letters, v. 34, p. 1363-

273   1165.

274 Pegoraro, A. F., Ridsdale, A., Moffat, D. J., Jia, Y., Pezacki, J. P., and Stolow, A., 2009,

275   Optimally chirped multimodal CARS microscopy based on a single Ti:sapphire

276   oscillator: Optics Express, v. 17, p. 2984-2996.

277 Slepkov, A. D., Ridsdale, A., Pegoraro, A. F., Moffat, D. J., and Stolow, A., 2010,

278   Multimodal CARS microscopy of structured carbohydrate biopolymers:

279   Biomedical Optics Express, v. 1, p. 1347-1357.

280 Slepkov, A. D., Ridsdale, A., Wan, H. N., Wang, M. H., Pegoraro, A. F., Moffatt, D. J.,

281   Pezacki, J. P., Kao, F. J., and Stolow, A., 2011, Forward-collected simultaneous

282   fluorescence lifetime imaging and coherent anti-Stokes Raman scattering

283   microscopy: Journal of Biomedical Optics, v. 16, no. 2.

284 Vanko, D. A., and Stakes, D. S., 1991, Fluids in oceanic layer 3: Evidence from veined

285   rocks, Hole 735B, southwest Indian Ridge, *in* Von Herzen, R. P., and Robinson,

286   P. T., eds., Proceedings of the Ocean Drilling Program, Scientific Results,

287   Volume 118: College Station, TX, Ocean Drilling Program, p. 181-215.
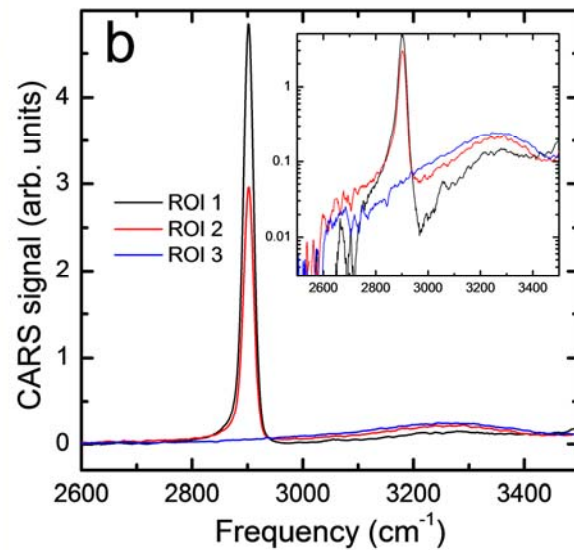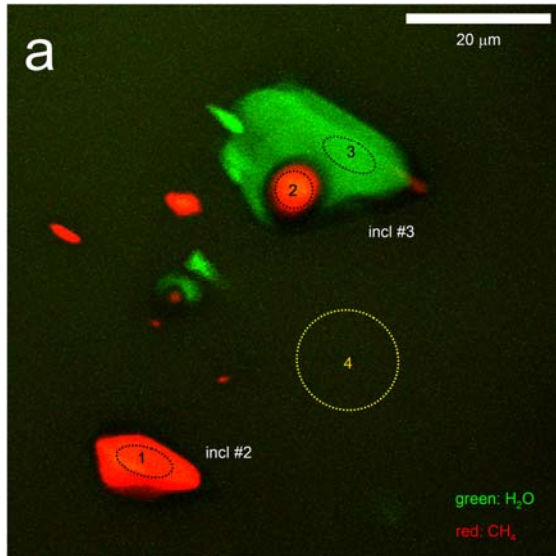
288

Fig. DR1. CARS image (a) and spectra (b) of methane and water in inclusions in text Fig.

3 and video DR3. The spectra of regions of interest (ROI) 1 to 3 in (a) were corrected for

nonresonant background signal sampled from ROI 4. The inset shows the spectra plotted

on a log-normal scale for clarity. We do not observe a spectrum for CH_4 dissolved in the

aqueous phase (ROI 3) in incl. #3 because of the quadratic dependence on the CARS

signal on concentration as discussed in the DR text. The presence of a water band in the

spectrum of the CH_4-rich vapor bubble in incl. #3 (ROI 2) may be due to factors such as

water vapor in the CH_4-rich phase and signal from the aqueous phase surrounding the
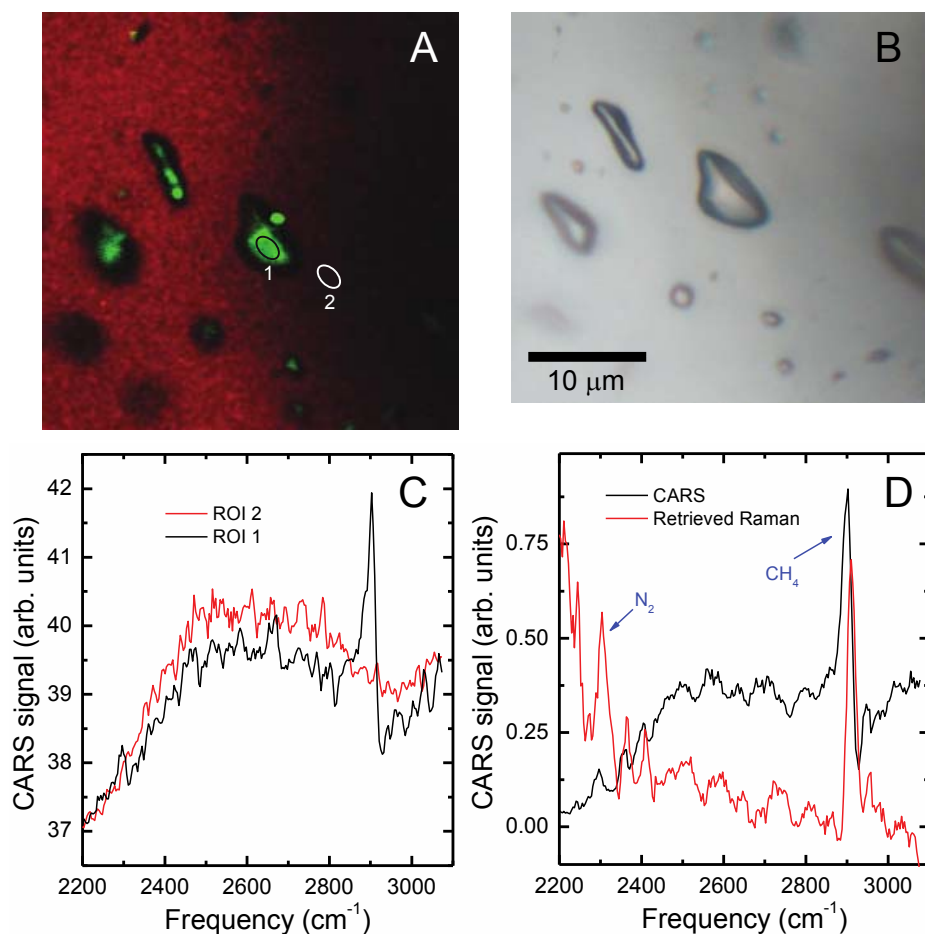
vapor phase.

Fig. DR2. CARS image and transmitted light image of one-phase CH_4-N_2 inclusions in
Sample 3 with raw and processed spectra. (A) The regions of interest (ROI) in the image
from which spectra were extracted are the numbered ovals. The green color is the TPEF
signal that most probably originates from high-molecular-weight aromatic molecules in
these inclusions. Although the inclusions formed under amphibolite facies metamorphic
P-T conditions, the traces of high-molecular-weight material in the inclusions may have
formed on cooling of a fluid initially in equilibrium with graphite. (B) transmitted light
image of inclusions in A (C) Raw CARS spectra from an inclusion and from the adjacent
matrix. (D) Processed CARS spectra with nonresonant background removed and further

317   converted to an approximate spontaneous Raman spectrum with a Kramers-Kronig

318   transformation-based algorithm (Liu et al., 2009).

319

320
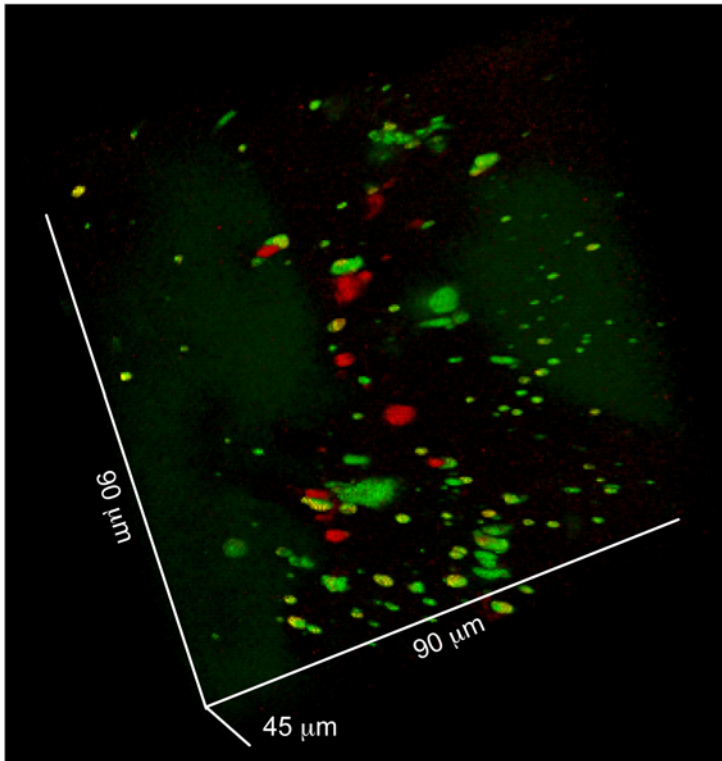
321
322
323
324
325
326   Fig. DR3. 2D image of 3D rendering (video DR4) of CH_4-rich inclusions within a

327   hornblende grain in Sample 4, fractured and hydrothermally altered basalt from oceanic

328   layer 3. CH_4-rich inclusions are shown in red. CH_4-rich inclusions that contain

329   fluorescent higher hydrocarbons and fluorescent mineral inclusions are colored green in

330   TPEF. Dimensions are given on the axes.

331

332

333

334